# Application of Gaussian and Percentile filters in Particle Swarm Optimisation for 3D gravity modelling and its implementation on Sinanpaşa graben gravity data in SW Turkey

A. B. Tekkeli, O. Tarhan Bal and G. Karcioğlu

*Geophysical Engineering Department, Engineering Faculty, Istanbul University - Cerrahpaşa, İstanbul, Turkey*

**ABSTRACT**    3D Modelling of gravity data is generally performed as a multi-objective optimisation, trying to minimise observed-calculated data misfit while providing models with certain properties, such as smooth or sharp boundaries. We demonstrated that controlling the model properties in global optimisation schemes is possible through basic image processing filters, and developed a Particle Swarm Optimisation (PSO) algorithm that benefits from Gaussian and Percentile filters to avoid ambiguous boundaries that are generally seen in 3D smooth inversions of gravity data. The effectiveness of the algorithm is shown on a synthetic model consisting of two dipping structures with anomalous density contrasts. Thereafter, the algorithm is implemented to recover subsurface density distribution from a field data set. The field data is collected at the south-western part of the Sinanpaşa graben, Turkey. Due to the lack of previous geophysical studies in the area, 3D Euler decomposition, tilt angle, and 3D smooth inversion methods are also implemented to help interpretation and to compare to the model recovered using the PSO algorithm. The developed approach is observed to be resulted with a model, which is more compatible with the known geology of the region.

**Key words:**    gravity modelling, Particle Swarm Optimisation, 3D inversion, 3D Euler decomposition, Sinanpaşa graben.

## 1. Introduction

Derivative based inversion methods are used widely to recover structure shapes and depths from gravity data. Numerous inversion schemes for determining simple geometries from gravity data are present in the literature (e.g. Chakravarthi and Sundararajan, 2004; Essa, 2013; Abdelrahman and Essa, 2015), however, a more complete picture of the subsurface can be obtained through 3D modelling, in which the entire data set is evaluated (e.g. Cella *et al.*, 2007; Khalil *et al.*, 2014; Witter *et al.*, 2016). The use of global optimisation methods for gravity modelling is implemented for more than a decade (e.g. Montesinos *et al.*, 2005, 2006; Berrino and Camacho, 2008; Pallero *et al.*, 2015, 2017; Singh and Singh, 2017; Ekinci *et al.*, 2021), and still increasing with the development of faster forward modelling algorithms and higher parallelisation capabilities of PCs.

The structures in the models obtained from 3D smooth inversion methods are generally

recovered with ambiguous boundaries, misleading fault dips and vertically exaggerated structures (Witter *et al.*, 2016), which are difficult to interpret. In the smooth inversion schemes, models with maximum possible smoothness are generally aimed and the level of smoothness is adjusted to increase fitting between the observed and the calculated data sets. However, sharper boundaries might be wanted in many geological scenarios (Mehanee and Zhdanov, 2002), making better control of the smoothness and sharpness necessary. In traditional inversion methods, sharper boundaries are often ensured by the implemented stabilising functional (e.g. Portniaguine and Zhdanov, 1999; Smith *et al.*, 2001; Mehanee and Zhdanov, 2002; Auken and Christiansen, 2004; de Groot-Hedlin and Constable, 2004; Zhao *et al.*, 2016; Guo *et al.*, 2017). Another method to overcome the mentioned problems is to use Bayesian methods. In these methods, a large amount of candidate models are determined and the probabilities of the recovered models are evaluated, yielding better estimations for the structure boundaries (e.g. Chen *et al.*, 2014; Ray *et al.*, 2014; Rossi *et al.*, 2015; de Pasquale *et al.*, 2019; Seillé and Visser, 2020). When the Global Optimisation methods are used, structural modelling approaches are generally implemented (e.g. Mohnke and Yaramanci, 2002; Akça and Başokur, 2010; Başokur and Akça, 2011).

In the algorithm used in this study, Gaussian and Percentile filters, which are generally used for image processing, are integrated into a Global Optimisation scheme to find a balance between smoothness and sharpness.

Gaussian filters are applied widely to smooth data. In geophysical inversion, smoothing operators are often scaled to account for the cell sizes. Correspondingly, the implemented Gaussian filter kernel is scaled according to the cell dimensions. The Percentile filter is also applied to filter low frequency effects without smoothing boundaries. The model parameters, obtained after the implementation of these two filters, are expected to be minimising the observed-calculated data misfit while providing relatively simple models with well-defined boundaries.

The developed modelling approach is implemented using Particle Swarm Optimisation (PSO), which is an evolutional global optimisation algorithm finding optimal solutions by trial and errors. Accordingly, the method starts from a randomised set of model parameters (density contrasts) and changes them in each iteration until the desired model fitness is achieved. In order to show the effectiveness of the developed algorithm, the method is implemented on a synthetic data set with two dipping structures. The structure boundaries obtained using PSO with Gaussian and Percentile filters are observed to be closer to that of the actual model. Thereafter, the algorithm is applied on a field data set collected in the south-western part of the Sinanpaşa graben in Turkey.

For comparison, the data are also modelled in 3D using a derivative based smooth inversion approach. Since the true structure of the Sinanpaşa graben is unknown, the data is also interpreted using 3D Euler deconvolution and tilt angle methods, which are used widely for preliminary interpretation of the gravity anomalies (e.g. Salem *et al.*, 2005; Drahor and Berge, 2006; Oruç and Keskinsezer, 2008; Oruç, 2011; Tedla *et al.*, 2011; Oruç *et al.*, 2013; Kıyak *et al.*, 2015; Ghosh, 2016).

## 2. Methods

### 2.1. PSO algorithm

PSO is a trial-error based evolutionary global optimisation algorithm developed by Kennedy and Eberhart (1995). The algorithm starts from a number of randomly generated initial models, which is called the population, and parameters in these models are updated iteratively to find

an optimal solution. Basically, PSO is the algorithm setting the rules to update these parameters.

For a population of $N$ models, the $n^{th}$ model with $M$ model parameters can be defined with a model parameter vector $m_n = m_{n,1}, m_{n,2}, ..., m_{n,M}$. For the gravity modelling case, $m_n$ consists of density contrast values associated to each cell. In our implementation, rectangular prism cells are used for discretising the subsurface.

Starting models are generally not employed in PSO and other similar global optimisation algorithms (e.g. genetic algorithms); however, a priori information is usually available in geophysics from geology or previous studies and valued greatly due to the non-uniqueness of the solutions. According to our trials, using an initial population randomly scattered around a user defined starting model ($m_0$) with the assumed background density contrast decreases the time consumption significantly and helps algorithm to avoid local minima. In our studies with synthetic and field data, we assumed $m_0 = m_{0,1}, m_{0,2}, ..., m_{0,M} = 0$ g/cm$^3$ in case of no priori information. The initial parameters of the models, constituting the population, are generated as below:

$$m_n(i = 0) = m_0(i = 0) + 0.01r \qquad (1)$$

where $r = r_0, r_1, .., r_M$ is a vector of uniformly distributed random values between [-1, 1]. The multiplier of the random vector is chosen to be necessarily low to keep the starting population around the initial model. Higher values of this multiplier may cause loss of the a priori information. After the fitness of the models in the population is tested, parameters in each model are updated using the equations below (Clerc and Kennedy, 2002):

$$m_n(i + 1) = m_n(i) + V_n(i + 1) \qquad (2)$$

$$V_n(i + 1) = \chi \left[ V_n(i) + c_1 c \phi_1 \left( m_{n,best} - m_n \right) + c_2 c \phi_2 \left( m_{g,best} - m_n \right) \right] \qquad (3)$$

where $i$ is the iteration number, $\varphi_1$ and $\varphi_2$ are uniformly distributed random parameters between [0, 1]. The damping factor $\chi$ is applied to prevent fluctuations in model parameters and given in Eq. 4. The parameter $m_{n,best}$ is the best model parameters obtained for the $n^{th}$ model of the population (local best) and $m_{g,best}$ is the vector of best model parameters determined considering the entire population (global best). We used Eq. 5 as the cost function to evaluate the fitness of each model, and to determine $m_{n,best}$ and $m_{g,best}$.

$$\chi = 2k \Big/ \left| 2 - c - (c^2 - 4c)^{\frac{1}{2}} \right| \qquad (4)$$

where $c = c_1 + c_2$ and $c_1$ and $c_2$ are generally chosen to satisfy $c \geq 4$, and the value of the multiplier $k$ is selected between [0, 1]. In the study of Clerc and Kennedy (2002), an analysis of these parameters is realised and values leading to better convergence are determined. Accordingly, $c_1$ and $c_2$ are generally selected to be 2.05 and the value of $k$ is set to ~ 0.99994 to make $\chi$ equal to 0.7298 (e.g. de Oca et al., 2008, 2011; Li and Yao, 2011). These values are also adopted in this study.

In traditional inversions, model smoothness is often introduced into the minimised functional and it is assured with methods that need the Jacobian matrix. In global optimisation, Jacobian

is not needed and adding the smoothness into the cost function is generally impractical due to the time cost of realising multi-objective optimisation for smoothness and misfit. Another factor increasing the solution time is the number of independent model parameters. In order to decrease the solution time, low-pass filters can be introduced into the global optimisation schemes to adjust model properties and to increase the interconnection between the model parameters. In this study, Gaussian and Percentile filters are implemented for these purposes.

Gaussian filters are widely used for low-pass filtering. When these filters are scaled according to the cell dimensions, they become analogous to the smoothing matrices used in traditional inversion methods. On the other hand, Percentile filters are non-linear filters, eliminating high frequency variations while keeping the boundary information. These filters are introduced into the PSO algorithm by implementing the cost function, given below:

$$U = \left\{ \left\| Wg - WF \left[ P \left( G(m_n(i)) \right) \right] \right\|^2 \right\} \tag{5}$$

where: $W$ is the weighting matrix, $g$ is the vector of observed data, $F$ denotes the forward solution, $m_n(i)$ is the $n^{th}$ model in the $i^{th}$ iteration. Forward calculation is realised using $m_n(i)$ after applying Gaussian and Percentile filters, denoted with G and P, respectively. Accordingly, values in the vector $m_n$ are not treated as the actual model parameters; these parameters are expected to minimise the misfit after Gaussian and Percentile filtering, respectively. Flowchart of the developed PSO workflow is provided in Fig. 1a.

The main parameters of the algorithm are the amount of filtering, percentage value for the Percentile filter, the population count, and the maximum number of iterations. Among these parameters, the amount of the implemented Gaussian filter forces algorithm to yield smoother models. In this study a simple 3D Gaussian kernel with the size of (3×3×3) cells is implemented. Graphical representation of the filter is given in Fig. 1b.

For a cell with dimensions $w_x$, $w_y$, $w_z$ in $x$, $y$, $z$ directions, coefficients of the scaled filter kernel ($G$ in Eq. 5) are calculated as below:

$$\begin{aligned} A_1 &= w_z/(w_y + w_z) \\ A_2 &= w_z/(w_x + w_z) \\ A_3 &= 0.5 \left[ w_x/(w_x + w_z) + w_y/(w_y + w_z) \right]. \end{aligned} \tag{6}$$

The central coefficient is assigned as $A_0 = 0.5$ and the neighbouring coefficients $A_1$, $A_2$, and $A_3$ are normalised to yield:

$$2 \left( A_1 + A_2 + A_3 \right) = 0.5. \tag{7}$$

The coefficients are calculated separately for each cell and their values can be adjusted further to provide different amount of smoothness in each direction.

The smoothness of the geological boundaries depends on the geology and the amount of smoothness should be selected to satisfy the geological constraints of the study area. In this context, if lower smoothness is necessary, the Percentile filter, which is also a low-pass filter, can be applied to increase the interconnection without smoothing the boundaries.

Percentile filtering is often used in image processing to remove noise. The method is known to be removing high frequency effects while preserving boundaries (Ataman *et al.*, 1981). The method ranks the values in the defined window and replaces the central pixel with the value corresponding to the desired percentile. In this study, the Percentile filtering algorithm provided with the SciPy library (Virtanen *et al.*, 2020) is implemented. The Percentile filter works as a minimum filter for the percentile value of 0 and as a maximum filter for 100. Accordingly, when the percentile is set to 100, the filter returns the maximum value in the filter window and vice versa. When the percentile is set to 50, the filter becomes a median filter.

Applying Percentile filter as a median filter (50%) replaces the value of a cell with the median value of the surrounding cells in the window; however, if the lower or higher percentile values are used, parameters become biased to have lower or higher values, respectively. As the filter approaches to become a maximum or minimum filter, the amount of this bias increases and the models are recovered with higher contrasts between structures. For example, when a percentile of 100% is used (maximum filter), the value of any given cell is replaced with the maximum value encountered in the filter window, increasing the value of the given cell. Accordingly, choosing the percentile considering the density contrasts of the anomalous structures yields better results. Considering this, *a priori* information is necessary for the selection of an appropriate percentile value.

In this study, Gaussian and Percentile filters are applied recursively and its amount is determined by trial and errors. Using the smoothing operator recursively is also implemented in geophysical smooth inversion algorithms (e.g. Kelbert *et al.*, 2014). The size of the Gaussian and Percentile filter windows are set to be (3×3×3) cells since higher filter sizes resulted with the loss of detail. However, larger filter windows may be preferred when denser meshes are used. The Percentile filter is applied close to be a maximum filter since the main objective both for the synthetic and the field examples is to reveal relatively high density structures.

The population count defines the amount of models to be generated every iteration and its value directly affects the solution time. Even though, higher population counts increase the quality of the solutions, its effect decrease after an optimum value (Li and Yao, 2011). In this study, the population size is selected according to the approach given in Li and Yao (2011):

$$N = 4 + 3log(M) \qquad (8)$$

where *M* is the number of model parameters (density contrasts).

With the implemented approach, it was possible to limit the maximum number of iterations to be 3500 and the optimisation is stopped if the desired observed-calculated data misfit is met (Fig. 1a). In this study, the misfit is measured using Root Mean Square (RMS) error, which can be given as below:

$$RMS = \sqrt{\frac{\left(W_g(g - F[m])\right)^T \left(W_g(g - F[m])\right)}{ng}} \qquad (9)$$

where: *ng* is the size of the data vector, $W_g$ is the data weighting matrix, and *F*[*m*] is the calculated data for the model parameters (*m*).

The introduced filters and modelling parameters do not guarantee convergence or overcome non-uniqueness. The optimisation process can still stagnate due to the local minima, non-careful

selection of starting models or filtering parameters. These parameters should be selected and adjusted to reflect the known geological constraints and to minimise misfit between the observed and the calculated data. Due to the random nature of the PSO and the non-uniqueness of the problem, it is possible to obtain different results for the same data and optimisation parameters. The solutions are expected to be more robust with the implemented filters; however, obtaining different but generally similar solutions is still possible.
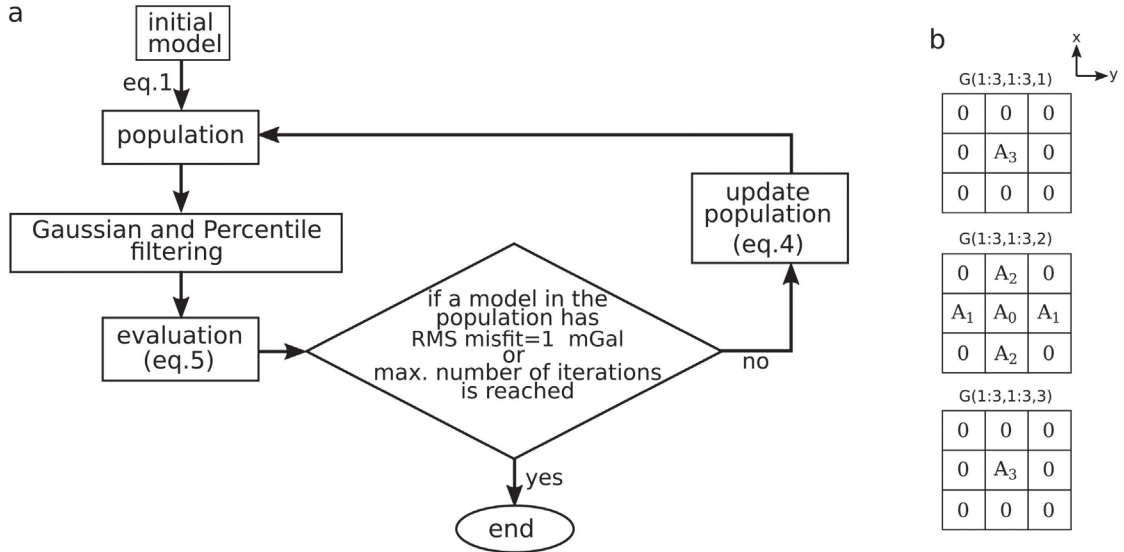


Fig. 1 - Flowchart of the PSO algorithm (a) and the graphical representation of the 3D Gaussian kernel with the size of (3×3×3) cells (b).

## 2.2. 3D smooth inversion

The inversion algorithm employed in this study discretises the subsurface using rectangular prism cells and the forward solutions are calculated using the equations provided in Li and Chouteau (1998). The implemented algorithm applies depth weighting as it is explained in Li and Oldenburg (1998).

Forward solution of gravity data can be defined as below:

$$F[m] = Jm \tag{10}$$

where $J$ is the matrix of coefficients defining the contributions from each cell to calculated data and $F[m]$ is the forward solution (calculated data) for the model parameter vector $m$. In gravity modelling, vector of model parameters consists of density contrast values associated to each cell.

In this study, inversion with smoothness constraint (Li and Oldenburg, 1998; Li, 2001; Farquharson, 2008) is implemented for the given gravity modelling problem. For the smooth inversion, the objective function to be minimised can be written as a sum of two components; least-squares misfit between the observed and calculated data, and the regularisation term

(Constable *et al.*, 1987; de Groot-Hedlin and Constable, 1990; Li and Oldenburg, 1998; Li, 2001). Accordingly, the objective function can be given as below:

$$U = \mu^{-1}\|Wg - WF(m)\|^2 + \|Cm\|^2 \tag{11}$$

where *W* is the weighting matrix; *F*(*m*) is the forward solution (calculated data) using the model parameters *m*. μ is the Lagrange coefficient, controlling the trade-off between smoothness and misfit; *C* is the regularisation term. In smooth inversion, regularisation is realised using matrices calculating differences between adjacent model cells and the model parameters satisfying the desired misfit between observed and calculated data can be found using:

$$m = \left[\mu\left(\partial_x^T\partial_x + \partial_y^T\partial_y + \partial_z^T\partial_z\right) + J^TW^TWJ\right]^{-1}J^TW^TWg \tag{12}$$

where: $\partial_x$, $\partial_y$, and $\partial_z$ denote matrices differencing adjacent cells (roughening matrices); *i* is the iteration number; *J* is the coefficient matrix; *g* is the observed data. In order to find the smoothest models with the required misfit, larger values of μ are applied. If the solution does not satisfy the condition for the misfit, is decreased, resulting with rougher models.

Due to the non-uniqueness of the problem, the solution recovered using the Eq. 12 may not be geologically reasonable. If there is *a priori* information about the densities of the subsurface structures, upper and lower limits for model parameters can be defined. These boundaries can be simply applied by setting the model parameters out of the limits to the defined boundary values (Chasseriau and Chouteau, 2003); however, the described process may increase observed-calculated data misfit, making the solution unacceptable. In this case, even though the gravity field at any point on the surface is linearly related to the model parameters in Eq. 10, iterative solutions are applied (Li, 2001; Chasseriau and Chouteau, 2003). Accordingly, new model parameters can be calculated using:

$$m_{i+1} = m_i + \left[\mu\left(\partial_x^T\boldsymbol{\partial_x} + \partial_y^T\boldsymbol{\partial_y} + \partial_z^T\boldsymbol{\partial_z}\right) + (WJ)^T(WJ)\right]^{-1}(WJ)^TW(g - F[m_i]) \tag{13}$$

where $F[m_i]$ denotes the forward solution using the current model parameters in the $i^{th}$ iteration $m_i$.

### 2.3. 3D Euler deconvolution and tilt angle calculations

The 3D Euler deconvolution (Reid *et al.*, 1990) and tilt angle (Miller and Singh, 1994) is applied widely on gravity data for detecting faults and lineaments:

$$(x - x_0)\frac{\partial}{\partial x}g_w(x,y,z) + (y - y_0)\frac{\partial}{\partial y}g_w(x,y,z) + (z - z_0)\frac{\partial}{\partial z}g_w(x,y,z) = -ng_w(x,y,z) \tag{14}$$

where $g_w(x, y, z)$ is the data in the applied window to be assumed due to a point source, which is located at $(x_0, y_0, z_0)$, and *n* is the Structural Index (SI) value associated with the assumed source geometry.

The 3D Euler deconvolution is essentially based on the Euler's inhomogeneity equation. The

method is applied to the residual potential field data with a data window, parsing ≥ 5 data points in each direction. By assuming point sources, location and depth information for the anomaly in the given data window is recovered from the least-squares solution of Eq. 14. Solutions for various point sources can be obtained by simply changing the SI. SI values for gravity data, corresponding to different point sources, are provided in Table 1. Detailed information about the implementation of the 3D Euler deconvolution method can be found in Reid *et al*. (1990), Stavrev (1997), FitzGerald *et al*. (2003), Silva and Barbosa (2003), Reid and Thurston (2014) and Reid *et al.* (2014).

Table 1 - Structural index values for gravity data (Reid *et al.*, 2014).

| Model | SI |
|---|---|
| Point, sphere | 2 |
| Line, cylinder, thin bed fault | 1 |
| Thin sheet edge, thin sill, thin dike | 0 |
| Thick sheet edge | -1 |

Tilt angle (θ) calculations are realised using the first derivatives of the data, using (Miller and Singh, 1994; Verduzco *et al.*, 2004):

$$\theta = tan^{-1} \left[ \frac{\left(\frac{\partial g}{\partial z}\right)}{\sqrt{\left(\frac{\partial g}{\partial x}\right)^2 + \left(\frac{\partial g}{\partial y}\right)^2}} \right].$$ (15)

The zero contours on the tilt angle maps indicate structure boundaries. In this study, calculation and mapping of the tilt angle values are realised using Potensoft software (Arisoy and Dikmen, 2011).

## 3. Implementation on synthetic data

The synthetic data set is generated from a model consisting of two dipping structures with anomalous density contrasts (Figs. 2a and 2b). Synthetic data is sampled in every 50 m in both directions (Fig. 2c) and 5% Gaussian noise is added before the modelling (Fig. 2d).

The synthetic data set is modelled using smooth inversion (Figs. 3a, 4a, 4b), PSO with Gaussian filter only (Figs. 3b, 4c, 4d), which can be considered analogous to smooth modelling, and PSO with Gaussian and Percentile filters (Figs. 3c, 4e, 4f), which is expected to yield better defined boundaries. In all modelling trials, density contrast values are forced to be > 0. We assumed, $m_0 = m_{0,1}, m_{0,2}, ..., m_{0,M} = 0$ g/cm$^3$ as the starting model, which corresponds to the true background density contrast.

According to our initial trials, applying low amount of filtering results with noisy looking models due to the low interconnection between the model parameters, and very high level of filtering results with oversimplified models. The level of Gaussian filter is adjusted to avoid

oversmoothing of the model parameters. The percentile filter is implemented with a high percentile value to increase the bias of the models parameters toward higher densities. After several tries, the Gaussian filter is applied 10 times recursively and the Percentile filter is applied using 95% percentile value. During the modelling, 5% error floor is assumed for data weighting and correspondingly the desired misfit is determined to be 1 mGal RMS to avoid fitting to the noise.

As result, all three models are obtained with 1 mGal RMS misfit. The model recovered using PSO algorithm with Gaussian and Percentile filters is observed to be reflecting the structures better since the oversmoothing is prevented and the parameters are biased to have higher density contrast values due to the effect of the percentile filter. Even though, the exact dips of the structures are not recovered in the model shown in Fig. 4f, the percentile filter observed to be keeping the structure boundaries relatively clear, even in the deeper parts of the model.
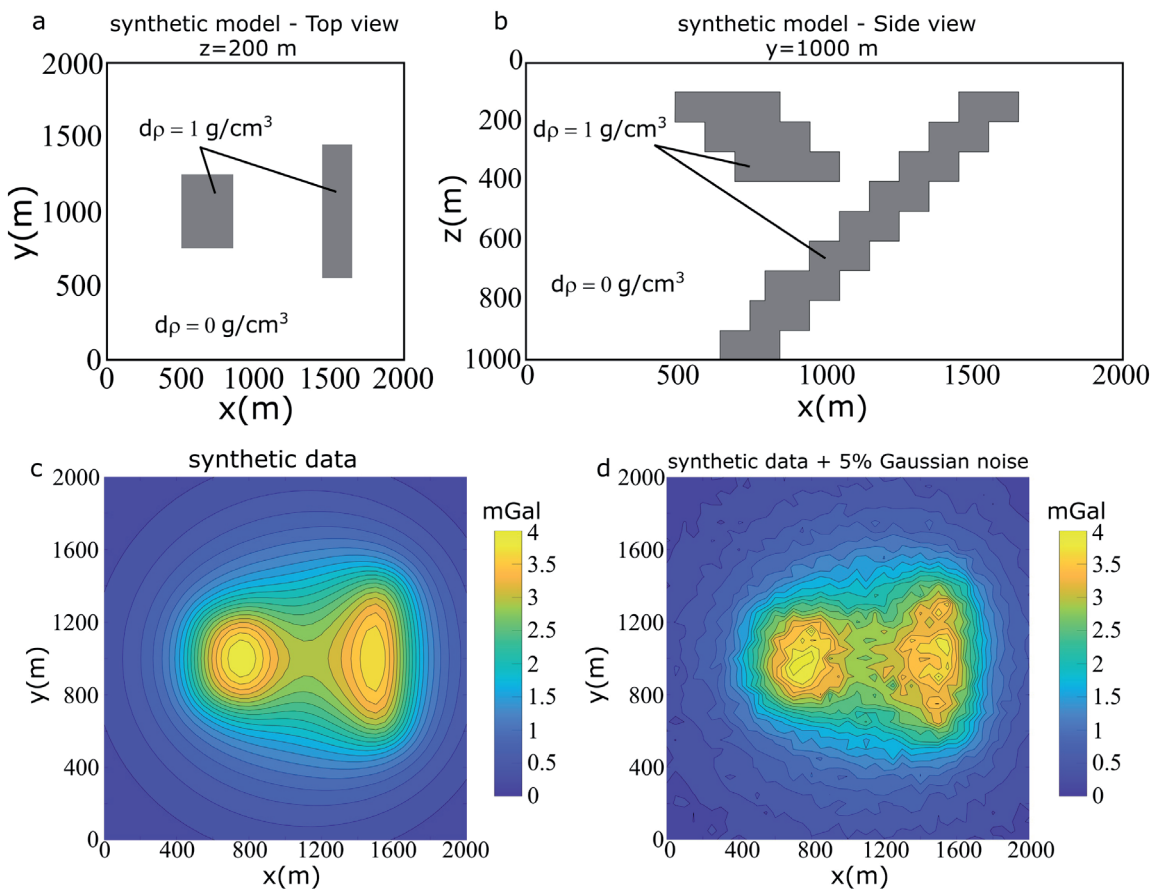


Fig. 2 - Top ($z$ = 200 m) and side view ($y$ = 1000 m) of the synthetic model, used for testing the developed algorithm, are given in panels a and b, respectively. The data, generated from the synthetic model, and the same data with 5% Gaussian noise are provided in panels c and d, respectively.
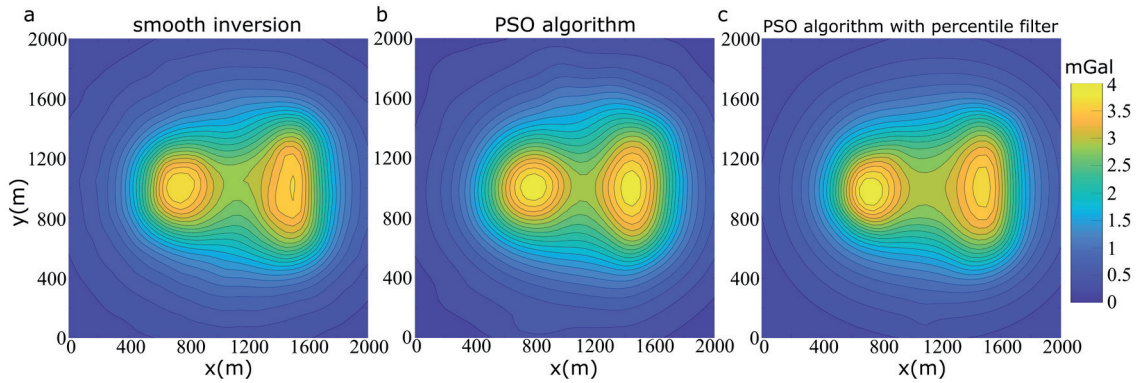
Fig. 3 - Data, calculated from the modelling results of the smooth inversion, PSO with Gaussian filter, and PSO with Gaussian and Percentile filters are shown in panels a, b, and c, respectively.
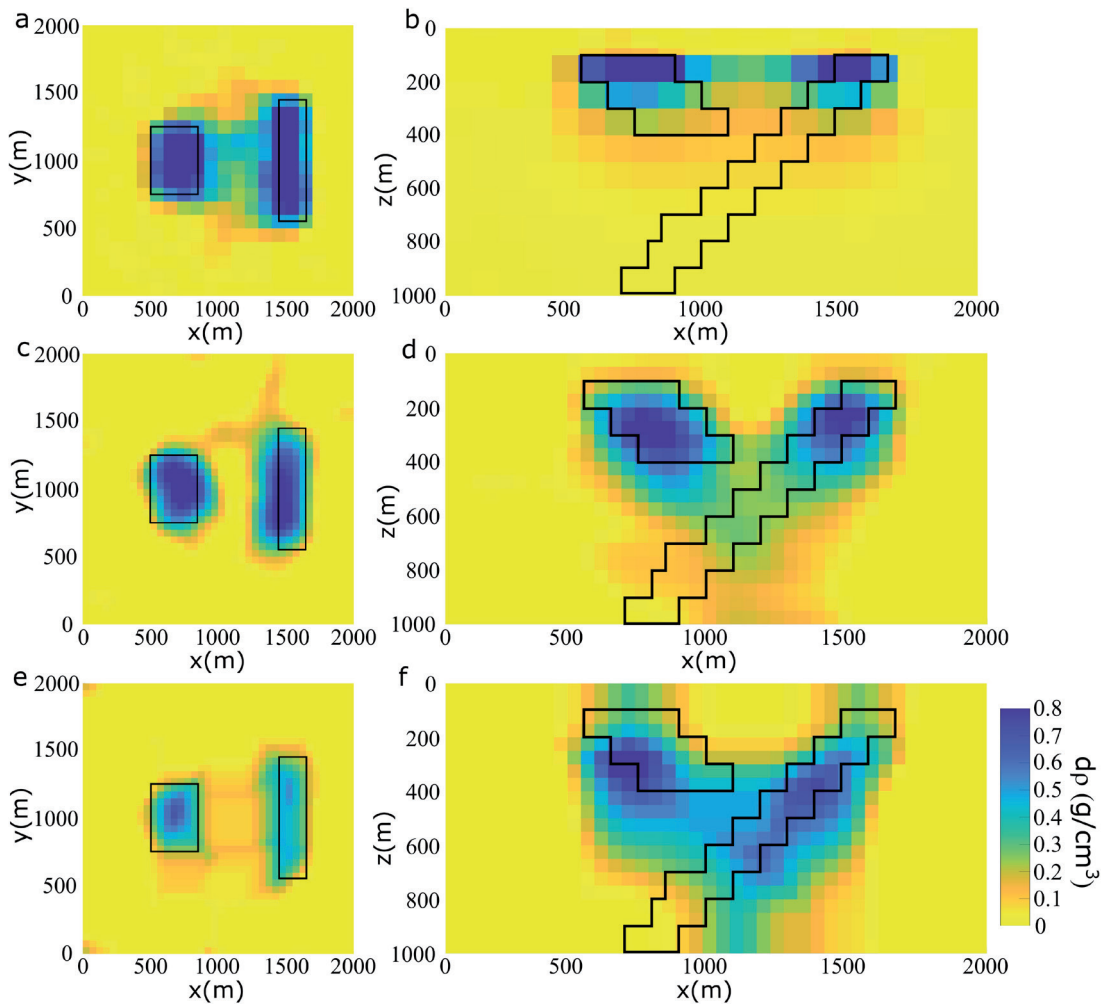


Fig. 4 - The top ($z$ = 200 m) and side views ($y$ = 1000 m) of the recovered models are given in panels a and b for smooth inversion, in panels c and d for PSO with Gaussian filter, and in panels e and f for PSO with Gaussian and Percentile filters.

## 4. Field data and geological setting

The field data set consists of vertical component gravity data (Fig. 5), collected on land in the western part of the Sinanpaşa graben in SW Turkey (Fig. 6) at 989 data points on a grid with 250-m intervals in both directions using a Scintrex CG-5 Autograv gravity meter. Bouguer and terrain corrections are realised by the contractor company, which granted the data, assuming a 2.3 g/cm$^3$ constant density. The main feature in the Bouguer anomaly map (Fig. 5) and the residual gravity data (Fig. 7a) is the transition from higher anomaly values in the SW to lower in the NE. The direction of this transition is compatible to the strike of the faults in the region (Fig. 6) and related topographic features (Fig. 7b).

The study area is a part of a graben system, located in western Anatolia, lying in the Aegean Extensional Province (AEP). Previous studies show that the region went under two extensional phases interrupted by a compressional episode (Koçyiğit, 2005; Koçyiğit and Deveci, 2007). The compressional regime between late Miocene and mid-Pliocene caused the development of the reverse and strike-slip faults in the region (Koçyiğit and Deveci, 2007; Gündoğdu et al., 2015). The latest Pliocene marks the starting of the neotectonic regime and many of the normal faults in the region are developed with the introduction of the present day NNE-SSW extensional regime. Due to the mentioned extension periods, a progressive inward development of normal faults is proposed (Alçiçek et al., 2005; Gürer et al., 2009) and may also be expected for the Sinanpaşa graben.

The study area encompasses the south-western part of the Sinanpaşa graben, which developed between Early Miocene and Pliocene (Akıska and Varol, 2020). The detailed geology maps of the study area (MTA, 2002, 2011) suggest that a large portion of the area is covered with the Miocene continental clastics and volcanics (Fig. 6), which are considered to be part of the N-S trending Kırka-Afyon-Isparta Alkaline Volcanic Assemblage (Savaşçin and Oyman, 1999).

Most of the Neogene basins in the region have a 0.5-3.0 km thickness, and according to Günen (2011), Quaternary sedimentary fill in Sinanpaşa graben is expected to be ~500 m. The basement of the Sinanpaşa basin is described with Paleozoic metamorphic rocks overlain by Mesozoic dolomitic limestone and marble (Candan et al., 2005; Akıska and Varol, 2020).
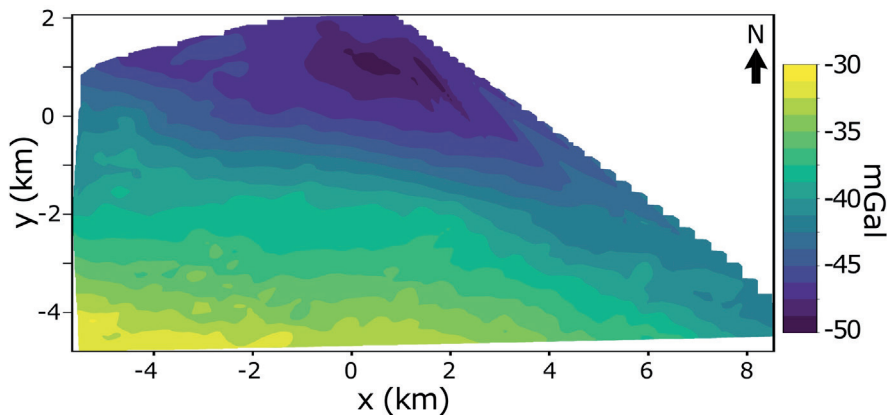


Fig. 5 - Bouguer anomaly map of the study area.

According to the active fault map of Emre et al. (2011), the eastern part of the 8.2 km long Elvanpaşa Segment (ES) of the Akşehir-Simav Fault Zone (ASFZ) resides nearly in the centre of the

study area, extending in a NW-SE trend. The study area lies in a seismic gap (Yildiz *et al.*, 2012), however, the focal mechanisms of the earthquakes around the study area show normal faulting with a small strike-slip component (Eyidoğan and Jackson, 1985; Altuncu-Poyraz, 2009; Irmak and Taymaz, 2009; Irmak, 2013; Altuncu-Poyraz *et al.*, 2014; Tiryakioğlu *et al.*, 2018), which is compatible with the defined present day oblique-slip normal faulting of the ASFZ (Koçyiğit and Deveci, 2007). In the study of Günen (2011), faults representing the ASFZ in the region are described as north-dipping active faults with earthquake potential.
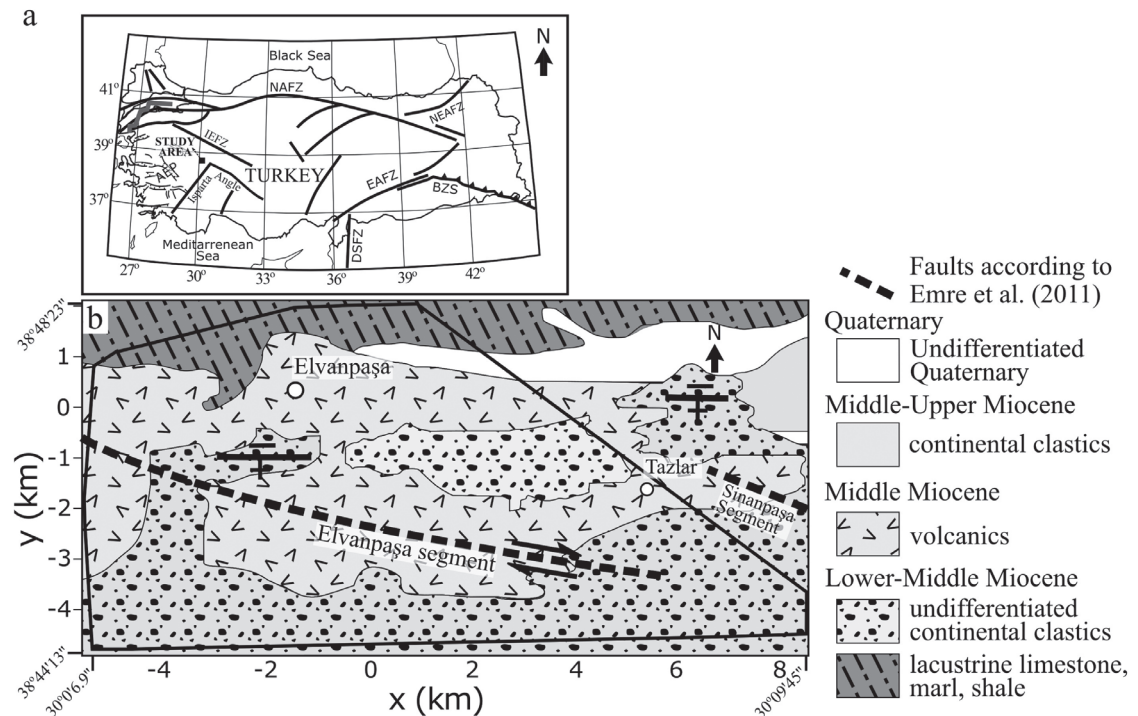


Fig. 6 - a) Major units controlling the neotectonics in Turkey. Location of the study area is shown with the black square. AEP: Aegean Extensional Province, NAFZ: North Anatolian Fault Zone, IEFZ: İnönü-Eskişehir Fault Zone, NEAFZ: North-East Anatolian Fault Zone, EAFZ: East Anatolian Fault Zone, BZS: Bitlis-Zagros Suture. b) Simplified geology of the study area (redrawn from MTA, 2002) and the main segments of the ASFZ system in the vicinity of the study area (Emre *et al.*, 2011). The normal faults in the area are shown according to the MTA (2011), and the footwall and the hanging-wall directions are indicated with '+' and '-', respectively. The boundaries of the area of measurement are shown with solid black lines.

## 5. Results and discussion

Interpretation of the field data is mainly realised using the recovered 3D models; 3D Euler and tilt angle methods are also implemented for comparison. The 3D Euler decomposition is implemented on the residual gravity anomaly (Fig. 7a) using a window encompassing 8 data points in both directions. SI = 0 is generally employed to detect boundaries due to faults. Hence, the SI space is not investigated, and only the results for SI = 0 are calculated and provided overlaying the topography (Fig. 7b). The tilt angle calculations are realised using Eq. 15 and provided in Fig. 7c.

Inversion of the data is realised using a mesh with 42,776 cells. The mesh consists of 34×54×25 cells for $z > 0$ and 11×17×6 cells for $z < 0$. The topography is incorporated into the mesh design. A homogeneous half-space initial model with the assumed background density contrast ( 0 g/cm$^3$) is employed. The inversion is stopped when RMS misfit of 1 mGal (Fig. 8a) is achieved according to the Eq. 9 and better fitting is not aimed to avoid fitting to the noise. Thereafter, the PSO algorithm is implemented using a mesh with 26×40×48 cells. After introducing the topography into the mesh, 32,291 model parameters are remained to be searched by the algorithm. The population count is determined to be N = 36. Filter parameters are determined after several trial and errors. As result, the Gaussian filter is determined to be applied 3 times recursively to filter low frequency changes, and 99% percentile value is determined to increase the contrast and to give a bias toward higher densities to prevent extension of the low density structures to the deep. The models in the starting population are randomly scattered around the assumed background density contrast (0 g/cm$^3$) using Eq. 1. Since a model with larger structures and sharper boundaries is aimed, relatively higher misfit between observed and calculated data is expected. The modelling is stopped after 1000 iterations and resulted with 1.38 mGal RMS misfit (Fig. 8b).

Plan views of the recovered models at $z$ = 350 m using smooth inversion and PSO algorithms are provided in Figs. 9a and 9b, respectively. Several S-N slices from the recovered models are shown in Fig. 10 for smooth inversion and in Fig. 11 for the PSO algorithms. In the mentioned figures, density contrasts depicting the deviation from the assumed background density of 2.3 g/cm$^3$ are provided.

3D Euler decomposition, tilt angle map, and the recovered 3D models indicate SE-NW and E-W trending boundaries, coherent with the strikes of the known faults and the lineaments observed through the topography (Fig. 7b). In the tilt angle map (Fig. 7c), the location of the ES is viewed clearly as a zero '0' anomaly at ~2 km south of Elvanpaşa town, however, 3D Euler solutions show only a few points in the direction of this fault. The ES is also observed in the recovered 3D models and shown in Figs. 9 to 11. In the figures, ES is imaged as passing through the south of the low density sediment fill, consistent with the general properties of the Sinanpaşa basin.

The 3D Euler solutions indicate a second fault (f1) in the north, passing through ~0.5 km south of the Elvanpaşa town, sub-parallel to the ES (Figs. 9 to 11). This fault is also evident from the tilt angle map (Fig. 7c) and corresponds to the southern boundary of the lowest anomaly values in the study area, observed in the north in Fig. 5. In the recovered models, the location of the f1 is observed to be approximately corresponding to the southern boundary of the Quaternary sediments. This fault is interpreted as a normal fault, responsible for the development of the inner basin area in the north.

The third feature, determined from the gravity data, is the nearly E-W trending fault (f2) in the southernmost part of the study area. This fault is clearly observed from 3D Euler solutions and also can be traced in the recovered models (Figs. 9 to 11). The N-S features determined between the faults f2 and ES are interpreted as connecting faults.

These results suggest that the horizontal boundaries are successfully determined using both 3D smooth inversion and the PSO algorithm. The smooth inversion model suggests a basin between the faults f2 and ES (Fig. 10). The area between these faults is located in an elevated area and the development of a basin structure is unexpected. The smooth inversion is also found to be unable to determine the depth of the low density sediments to the north (Fig. 10).
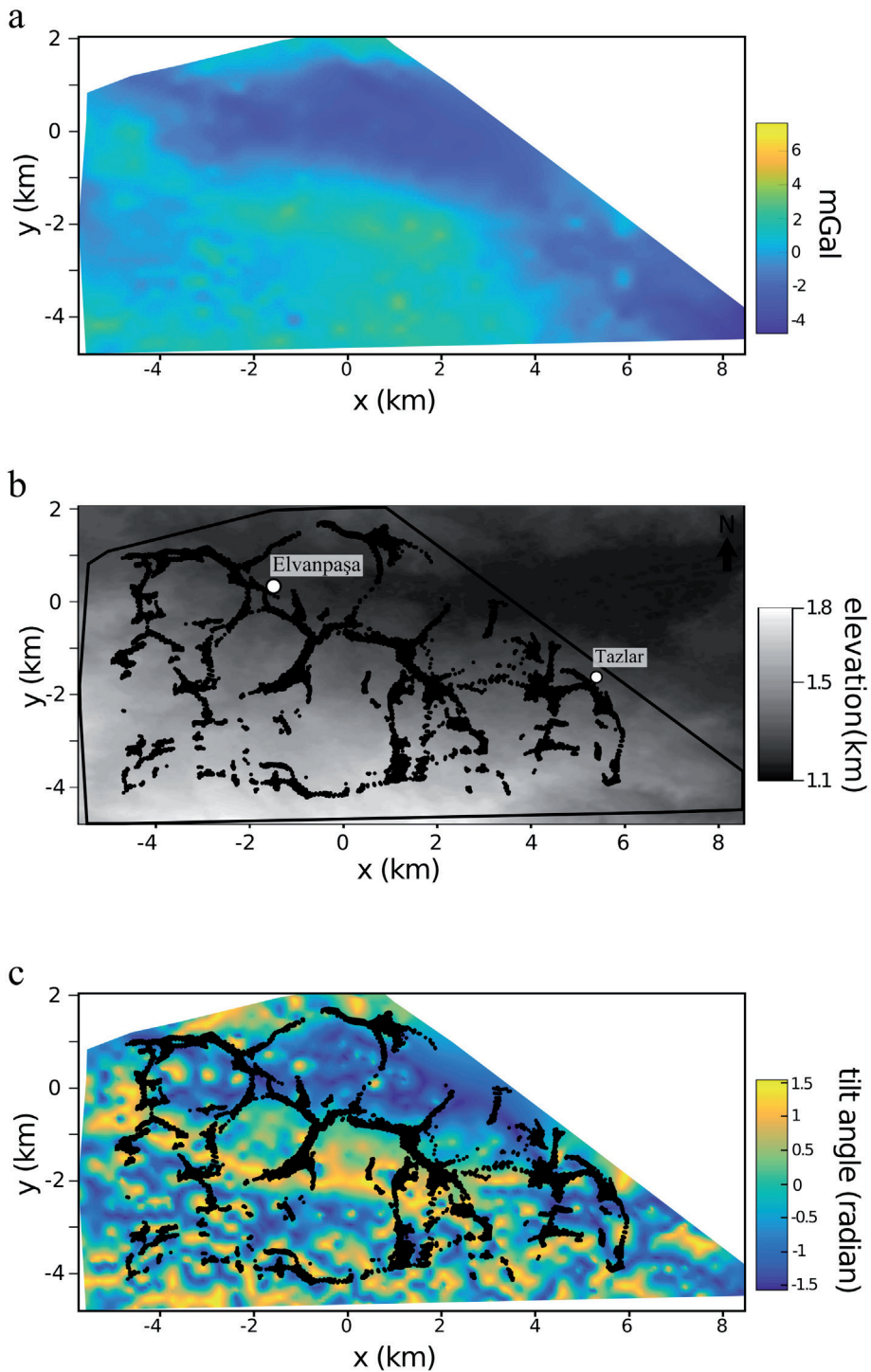
Fig. 7 - Residual anomaly map of the region (a), 3D Euler deconvolution solutions for the gravity data (shown with black circles) overlaying topography map (b) of the study area, and tilt angle calculations (c). The digital elevation model of the study area is produced by NASA/METI/AIST/Japan Space systems and U.S./Japan ASTER Science Team (2009).
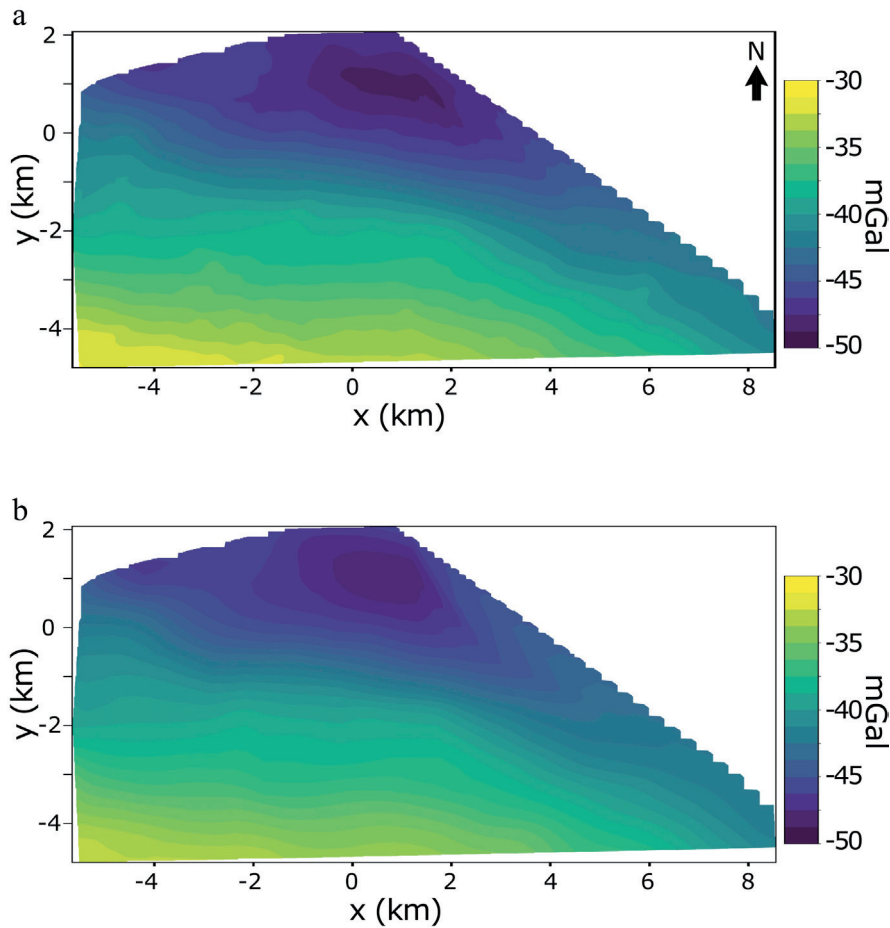
Fig. 8 - Calculated data for the models recovered using 3D smooth inversion (1 RMS) and PSO with Gaussian and Percentile filters (1.38 RMS) are given in (a) and (b) respectively.

The model recovered using the PSO algorithm with Gaussian and Percentile filters shows a picture better complying with the regional constraints (Fig. 11). Considering the geology of the Sinanpaşa basin, described in Akıska and Varol (2020), high density area ($d\rho$ > 0.2 g/cm$^3$) underlying low density rocks throughout the model is interpreted as the Paleozoic basement rocks. The regions with 0.1<$d\rho$< 0.2 g/cm$^3$ determined over the basement are interpreted as limestones and marbles.

In the model, the effect of the normal component of these faults are observed through the step-like changes in the basement topography, which are especially evident in the sections taken from the middle part of the model (Fig. 11, $x$ = -1, 0, 1, 2). The PSO algorithm also provided a better estimation for the sedimentary thicknesses. Accordingly, Miocene sediments overlying the high density basement in the south are determined to be ≤ 800 m thick and the lower density basin fill in the north is imaged with a thickness of ~1 km. The sediments in the south are recovered with relatively higher densities ($d\rho$ = 0 g/cm$^3$), which is consistent with the existence of Miocene volcanic and clastic rocks, while the lower density values determined in the north reflects the contribution of the Quaternary sediments.
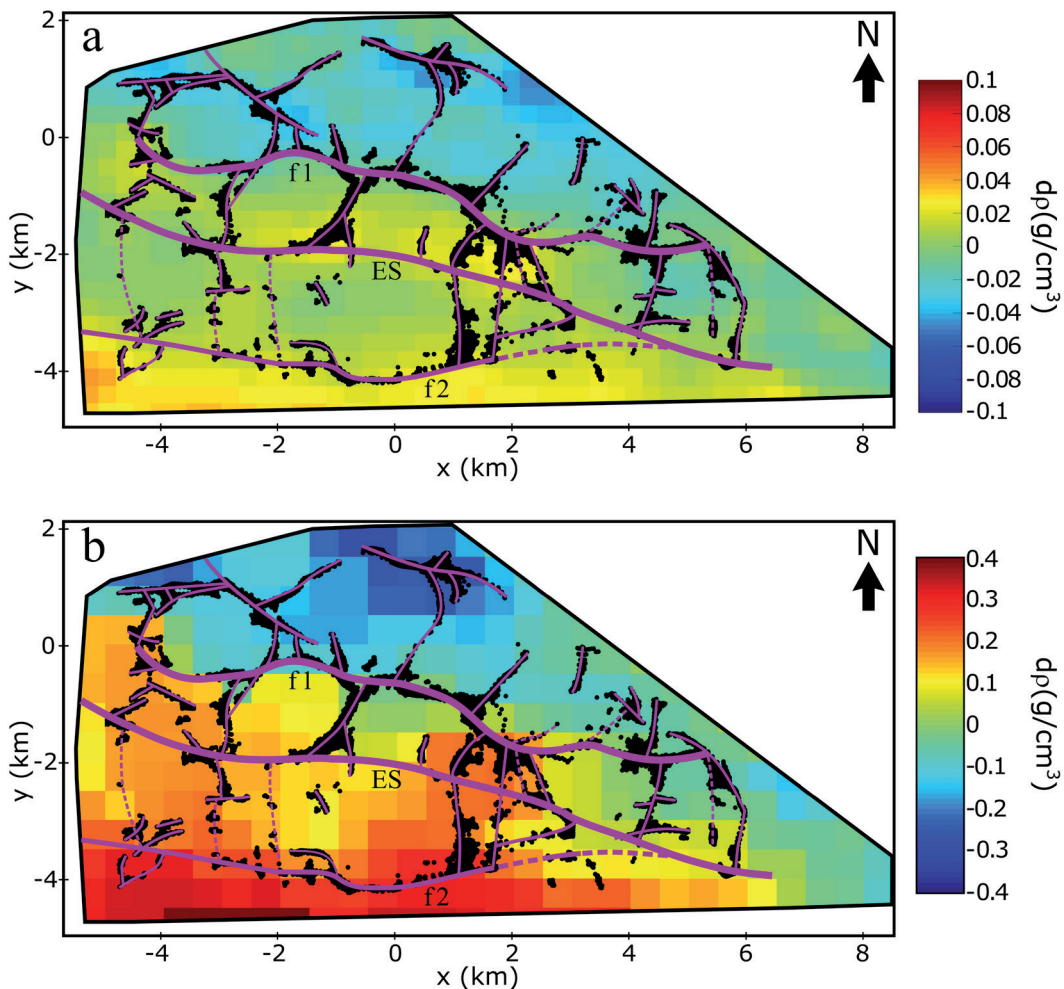
Fig. 9 - Plan view of the recovered model from 3D smooth inversion (a) and PSO modelling scheme (b) at *z* = 350 m. Prominent faults and lineaments interpreted from 3D Euler solutions (black circles) and tilt angle map (Fig. 7c) are shown with purple lines.

## 6. Summary and conclusions

In traditional inversion, smoothness of the boundaries between different geological structures is often tweaked to adjust the resulting misfit. However, properties of boundaries should be introduced into the modelling process as *a priori* information, based on the geology. In order to obtain 3D gravity distribution models while providing better control on the boundary properties, a PSO algorithm employing low-pass Gaussian and Percentile filters is developed. The implementation of these low-pass filters eliminates high frequency changes, increasing the interconnection between the neighbouring model parameters and reducing the time consumption of the algorithm.

Among these filters, low-pass Gaussian filter is applied to obtain smoothly varying model parameters. When models with lower smoothness are wanted, Percentile filter can be applied to increase the necessary interconnection between the model parameters while keeping the
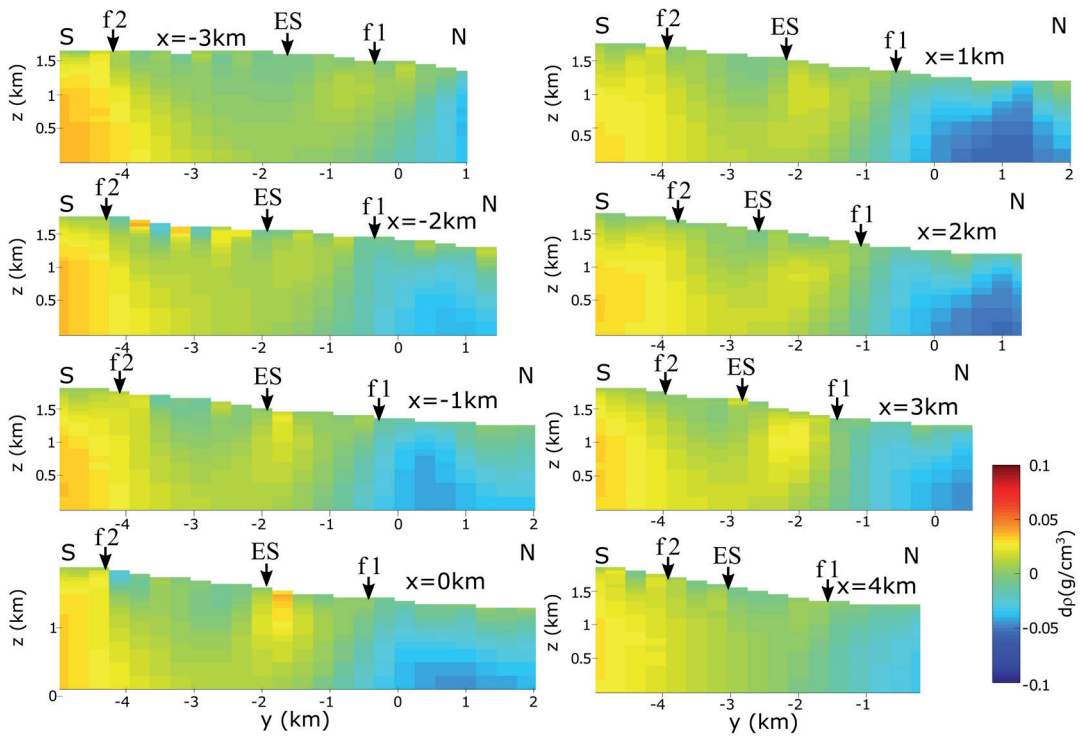
Fig. 10 - Cross-sections of the 3D smooth inversion model (1 RMS), taken at *x* = -3, -2, -1, 0, 1, 2, 3, and 4 km in S-N direction. Locations of the faults are shown using arrows. ES: Elvanpaşa segment.
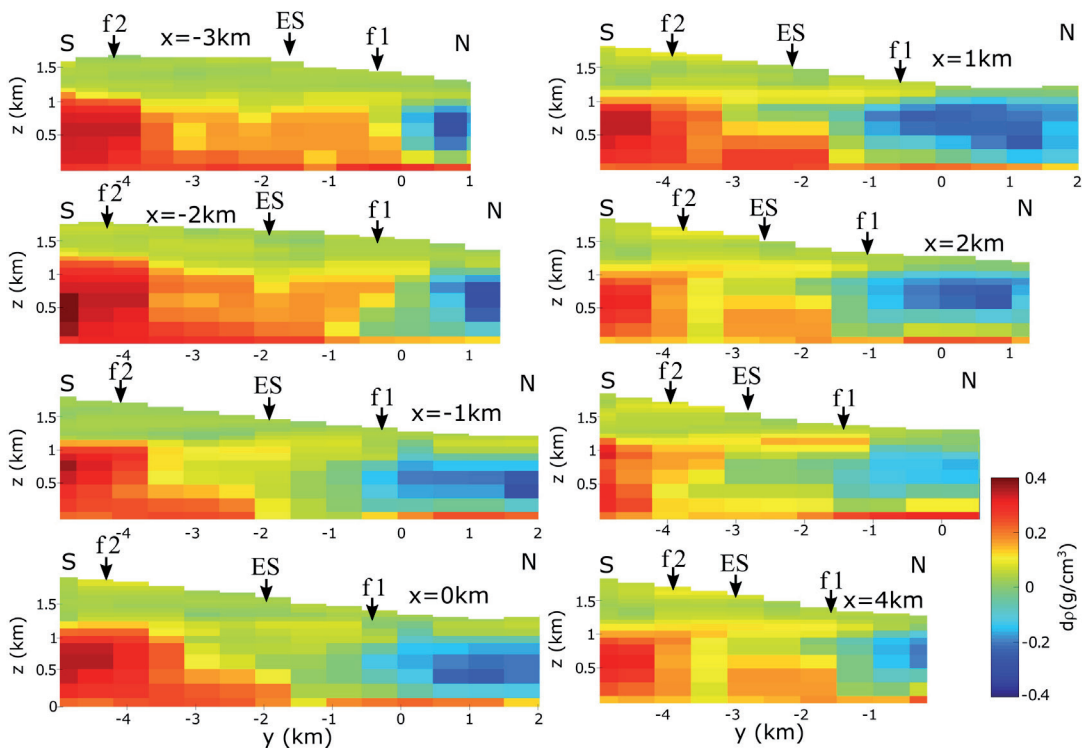


Fig. 11 - Cross-sections of the 3D PSO model (1.38 RMS), taken at *x* = -3, -2, -1, 0, 1, 2, 3, and 4 km in S-N direction. Locations of the faults are shown using arrows. ES: Elvanpaşa segment.

boundary information. The Percentile filter also can introduce a bias into the model parameters towards higher or lower density contrasts according to the chosen percentile value. The parameters of the Gaussian and Percentile filters are adjusted by trial and error to obtain models obeying geological constraints.

Initial tests on synthetic models show that the algorithm manages to minimise observed-calculated data misfit and provide models with better defined boundaries. Then, the algorithm is implemented on the vertical gravity data set collected on a grid with 250-m intervals in the western part of the Sinanpaşa graben in Turkey. For comparison, the data set is also evaluated using tilt angle, 3D Euler deconvolution, and 3D smooth inversion methods.

The tilt angle and 3D Euler solutions are observed to be indicating three main faults. The fault shown with f1 in Figs. 9 to 11 is observed to be forming the southern boundary of the area with the lowest density values. This fault is interpreted as a normal fault, controlling the inner basin area with low density Quaternary sediment fill. In the south, the fault f2 is observed to be bounding the area with the highest density values and forms the southern boundary of the Miocene volcanic units. This fault is observed to be converging to the ES to the east. These faults are also observed as horizontal boundaries in the smooth inversion and PSO models, showing that the horizontal boundaries are recovered successfully by the both methods.

Smooth inversion result suggests a basin area between the faults f2 and ES, which is not supported by the known geology of the area (Fig. 10). On the contrary, this basin is not recovered in the model obtained through the PSO algorithm. In Fig. 11, this area is imaged as Miocene sediments with a thickness of less than, or equal to, 800 m, overlying high density basement structure, and the faults f2 and ES are obtained as normal faults with observable hanging and foot walls. Smooth inversion result also suggests sedimentary thicknesses exceeding a 2-km depth in the north, which also contradicts the known geology. When the result of the PSO algorithm is considered, the thickness of these units are observed to be ~1 km, which agrees better with the geological characteristics of the area of investigation.

Both synthetic and field data implementations of the PSO algorithm show that the method benefits from the use of Gaussian and Percentile filters to obtain geologically consistent models with well-defined boundaries, avoiding problems of smooth inversions. The ease of implementation of these filters to control model properties also gives the freedom of using the same global optimisation algorithm for a wide range of problems, including smooth and sharp boundary modelling, by only changing the filters to be applied.

REFERENCES

Abdelrahman E.M. and Essa K.S.; 2015: *Three least-squares minimisation approaches to interpret gravity data due to dipping faults.* Pure Appl. Geophys., 172, 427-438.

Akça I. and Basokur A.T.; 2010: *Extraction of structure-based geoelectric models by hybrid genetic algorithms.* Geophys., 75, F15-F22.

Akıska E. and Varol B.E.; 2020: *Alluvial-lacustrine sedimentation and volcaniclastic deposition in an intracontinental tectonic graben: paleoenvironmental evolution of the Neogene Sinanpaşa basin, west-central Turkey.* Turk. J. Earth Sci., 29, 295-324.

Alçiçek M.C., Kazancı N. and Özkul M.; 2005: *Multiple rifting pulses and sedimentation pattern in the* Çameli *basin, southwestern Anatolia, Turkey.* Sediment. Geol., 173, 409-431.

Altuncu-Poyraz S.; 2009: *Isparta büklümünü oluşturan tektonik yapıların sismolojik yöntemlerle araştırılması*. PH.D. Thesis in Geophysics, İstanbul University, Istanbul, Turkey, 122 pp.

Altuncu-Poyraz S., Pinar A., Özden S. and Tunçer M.K.; 2014: *Implications of 2007's earthquake activity in Eğirdir Lake (SW Anatolia) based on moment tensor solutions and inversion of stress state.* Pure Appl. Geophys., 171, 1299-1309.

Arisoy M.Ö. and Dikmen Ü.; 2011: *Potensoft: MATLAB-based software for potential field data processing, modelling and mapping*. Comput. Geosci., 37, 935-942.

Ataman E., Aatre V. and Wong K.; 1981: *Some statistical properties of median filters*. IEEE Trans. Acoust. Speech Signal Process., 29, 1073-1075, doi: 10.1109/TASSP.1981.1163659.

Auken E. and Christiansen A.V.; 2004: *Layered and laterally constrained 2D inversion of resistivity data*. Geophys., 69, 752-761.

Başokur A.T. and Akca I.; 2011: *Object-based model verification by a genetic algorithm approach: application in archeological targets*. J. Appl. Geophys., 74, 167-174.

Berrino G. and Camacho A.G.; 2008: *3D gravity inversion by growing bodies and shaping layers at Mt. Vesuvius (southern Italy)*. Pure Appl. Geophys., 165, 1095-1115.

Candan O., Çetinkaplan M., Oberhänsli R., Rimmelé G. and Akal C.; 2005: *Alpine high-P/low-T metamorphism of the Afyon zone and implications for the metamorphic evolution of western Anatolia, Turkey*. Lithos, 84, 102-124.

Cella F., Fedi M., Florio G., Grimaldi M. and Rapolla A.; 2007: *Shallow structure of the Somma-Vesuvius volcano from 3D inversion of gravity data.* J. Volcanol. Geotherm. Res., 161, 303-317.

Chakravarthi V. and Sundararajan N.; 2004: *Ridge-regression algorithm for gravity inversion of fault structures with variable density*. Geophys., 69, 1394-1404.

Chasseriau P. and Chouteau M.; 2003: *3D gravity inversion using a model of parameter covariance*. J. Appl. Geophys., 52, 59-74.

Chen J., Hoversten G.M. and Nordquist G.; 2014: *Stochastic inversion of 2D magnetotelluric data using pixel-based parameterization*. In: Expanded Abstracts SEG Technical Program 2014, Denver, CO, USA, pp. 727-732, doi: 10.1190/segam2014-0071.1.

Clerc M. and Kennedy J.; 2002: *The particle swarm-explosion, stability, and convergence in a multidimensional complex space*. IEEE Trans. Evol. Comput., 6, 58-73.

Constable S.C., Parker R.L. and Constable C.G.; 1987: *Occam's inversion: a practical algorithm for generating smooth models from electromagnetic sounding data*. Geophys., 52, 289-300.

de Groot-Hedlin C. and Constable S.; 1990: *Occam's inversion to generate smooth, two-dimensional models from magnetotelluric data*. Geophys., 55, 1613-1624.

de Groot-Hedlin C. and Constable S.; 2004: *Inversion of magnetotelluric data for 2D structure with sharp resistivity contrasts*. Geophys., 69, 78-86.

de Oca M.A.M., Van den Enden K. and Stützle T.; 2008: *Incremental particle swarm-guided local search for continuous optimization*. In: Proc. 5th International Workshop on Hybrid Metaheuristics, Malaga, Spain, pp. 72-86, doi: 10.1007/978-3-540-88439-2_6.

de Oca M.A.M., Aydın D. and Stützle T.; 2011: *An incremental particle swarm for large-scale continuous optimisation problems: an example of tuning-in-the-loop (re) design of optimisation algorithms*. Soft Comput., 15, 2233-2255.

de Pasquale G., Linde N., Doetsch J. and Holbrook W.S.; 2019: *Probabilistic inference of subsurface heterogeneity and interface geometry using geophysical data*. Geophys. J. Int., 217, 816-831.

Drahor M.G. and Berge M.A.; 2006: *Geophysical investigations of the Seferihisar geothermal area, western Anatolia, Turkey*. Geotherm., 35, 302-320.

Ekinci Y.L., Balkaya Ç., Göktürkler G. and Özyalın Ş.; 2021: *Gravity data inversion for the basement relief delineation through global optimisation: a case study from the Aegean graben system, western Anatolia, Turkey*. Geophys. J. Int., 224, 923-944.

Emre Ö., Duman T.Y., Özalp S., Olgun Ş. and Elmacı H.; 2011: *1:250,000 scale active fault map series of Turkey, Afyon (NJ 36-5) quadrangle*. General Directorate of Mineral Research and Exploration, Ankara, Turkey, Serial Number: 16.

Essa K.S.; 2013: *Gravity interpretation of dipping faults using the variance analysis method*. J. Geophys. Eng., 10, 015003, 7 pp., doi: 10.1088/1742-2132/10/1/015003.

Eyidoğan H. and Jackson J.; 1985: *A seismological study of normal faulting in the Demirci, Alaşehir and Gediz earthquakes of 1969-70 in western Turkey: implications for the nature and geometry of deformation in the continental crust*. Geophys. J. Int., 81, 569-607.

Farquharson C.G.; 2008: *Constructing piecewise-constant models in multidimensional minimum-structure inversions*. Geophys., 73, K1-K9.

FitzGerald D., Reid A. and McInerney P.; 2003: *New discrimination techniques for Euler deconvolution*. In: Proc. 8th South Africa Geophysical Association Biennial Technical Meeting and Exhibition, Pilanesberg, South Africa, cp-144-00024, 9 pp., doi: 10.1016/j.cageo.2004.03.006.

Ghosh G.K.; 2016: *Interpretation of gravity data using 3D Euler deconvolution, tilt angle, horizontal tilt angle and source edge approximation of the north-west Himalaya*. Acta Geophys., 64, 1112-1138.

Gündoğdu E., Özden S. and Güngör T.; 2015: *Simav (Kütahya) ve yakın civarının Geç Senozoyik yaşlı jeodinamik evrimi*. Türkiye Jeoloji Bülteni, 58, 23-37.

Günen E.Y.; 2011: *Sincanlı Afyon Neojen havzası birimlerinin sedimantolojisi.* PH.D. Thesis in Natural and Applied Sciences, Ankara University, Ankara, Turkey, 200 pp.

Guo R., Wu X., Liu L., Li J., Xiao P. and Fang G.; 2017: *Adaptive sharp boundary inversion for transient electromagnetic data*. Prog. Electromagnet. Res., 57, 129-138.

Gürer Ö.F., Sarica-Filoreau N., Özburan M., Sangu E. and Doğan B.; 2009: *Progressive development of the Büyük Menderes graben based on new data, western Turkey*. Geol. Mag., 146, 652-673.

Irmak T.S.; 2013: *Focal mechanisms of small-moderate earthquakes in Denizli graben (SW Turkey)*. Earth, Planets and Space, 65, 943-955, doi: 10.5047/eps.2013.05.011.

Irmak T.S. and Taymaz T.; 2009: *Source mechanics of recent moderate earthquakes occurred in Honaz-Denizli (W Turkey) graben obtained by regional broadband waveform inversion*. In: Proc. International Symposium on Historical Earthquakes and Conservation of Monuments in the Eastern Mediterranean Region, Istanbul, Turkey, pp. 350-356.

Kelbert A., Meqbel N., Egbert G.D. and Tandon K.; 2014: *ModEM: a modular system for inversion of electromagnetic geophysical data*. Comput. Geosci., 66, 40-53.

Kennedy J. and Eberhart R.; 1995: *Particle swarm optimization*. In: Proc. ICNN'95 - International Conference on Neural Networks, Vol. 4, pp. 1942-1948, doi: 10.1109/ICNN.1995.488968.

Khalil M.A., Santos F.M. and Farzamian M.; 2014: *3D gravity inversion and Euler deconvolution to delineate the hydro-tectonic regime in El-Arish area, northern Sinai Peninsula*. J. Appl. Geophys., 103, 104-113.

Kıyak A., Karavul C., Gülen L., Pekşen E. and Kılıç A.R.; 2015: *Assessment of geothermal energy potential by geophysical methods: Nevşehir region, central Anatolia*. J. Volcanol. Geotherm. Res., 295, 55-64.

Koçyiğit A.; 2005: *The Denizli graben-horst system and the eastern limit of western Anatolian continental extension: basin fill, structure, deformational mode, throw amount and episodic evolutionary history, SW Turkey*. Geodin. Acta, 18, 167-208.

Koçyiğit A. and Deveci Ş.; 2007: *A NS-trending active extensional structure, the* Şuhut *(Afyon) graben: commencement age of the extensional neotectonic period in the Isparta Angle, SW Turkey*. Turk. J. Earth Sci., 16, 391-416.

Li X. and Chouteau M.; 1998: *Three-dimensional gravity modelling in all space*. Surv. Geophys., 19, 339-368.

Li X. and Yao X.; 2011: *Cooperatively coevolving particle swarms for large scale optimisation*. IEEE Trans. Evol. Comput., 16, 210-224.

Li Y.; 2001: *3-D inversion of gravity gradiometer data*. In: Expanded Abstracts SEG Technical Program 2001, San Antonio, TX, USA, pp. 1470-1473, doi: 10.1190/1.1816383.

Li Y. and Oldenburg D.W.; 1998: *3-D inversion of gravity data*. Geophys., 63, 109-119.

Mehanee S. and Zhdanov M.; 2002: *Two-dimensional magnetotelluric inversion of blocky geoelectrical structures*. J. Geophys. Res.: Solid Earth, 107, EPM 2-1-EPM 2-11, doi: l0.1029/2001JB000191.

Miller H.G. and Singh V.; 1994: *Potential field tilt - A new concept for location of potential field sources*. J. Appl. Geophys., 32, 213-217.

Mohnke O. and Yaramanci U.; 2002: *Smooth and block inversion of surface NMR amplitudes and decay times using simulated annealing*. J. Appl. Geophys., 50, 163-177.

Montesinos F.G., Arnoso J. and Vieira R.; 2005: *Using a genetic algorithm for 3-D inversion of gravity data in Fuerteventura (Canary Islands)*. Int. J. Earth Sci., 94, 301-316.

Montesinos F.G., Arnoso J., Benavent M. and Vieira R.; 2006: *The crustal structure of El Hierro (Canary Islands) from 3-D gravity inversion*. J. Volcanol. Geotherm. Res., 150, 283-299.

MTA (General Directorate of Mineral Research and Exploration); 2002: *Geological maps of Turkey, Ankara Raster*. Mustafa Şenel (ed), General Directorate of Mineral Research and Exploration, Geological Research Department, Ankara, Turkey, Scale 1:500,000.

MTA (General Directorate of Mineral Research and Exploration); 2011: *Geological maps of Turkey, Afyon K-24 Raster*. Erişen B. - Uysallı H. (1971), Kartal T. (1971), Karamanderesi İ.H. (1972), Bulduk A. (1986), Çakmakoğlu A. (1986), Turkey Geological Database, General Directorate of Mineral Research and Exploration, Geological Research Department, Ankara, Turkey, Scale 1:100,000.

NASA/METI/AIST/Japan Space systems, and U.S./Japan ASTER Science team; 2009: *ASTER Global Digital Elevation Model (GDEM)*. NASA EOSDIS Land Processes DAAC, doi: 10.5067/ASTER/ASTGTM.002.

Oruç B.; 2011: *Edge detection and depth estimation using a tilt angle map from gravity gradient data of the Kozaklı - Central Anatolia region, Turkey*. Pure Appl. Geophys., 168, 1769-1780.

Oruç B. and Keskinsezer A.; 2008: *Structural setting of the northeastern Biga Peninsula (Turkey) from tilt derivatives of gravity gradient tensors and magnitude of horizontal gravity components*. Pure Appl. Geophys., 165, 1913-1927.

Oruç B., Sertçelik I., Kafadar Ö. and Selim H.H.; 2013: *Structural interpretation of the Erzurum basin, eastern Turkey, using curvature gravity gradient tensor and gravity inversion of basement relief*. J. Appl. Geophys., 88, 105-113.

Pallero J.L.G., Fernandez-Martinez J.L., Bonvalot S. and Fudym O.; 2015: *Gravity inversion and uncertainty assessment of basement relief via particle swarm optimisation*. J. Appl. Geophys., 116, 180-191.

Pallero J.L.G., Fernandez-Martinez J.L., Bonvalot S. and Fudym O.; 2017: *3D gravity inversion and uncertainty assessment of basement relief via particle swarm optimisation*. J. Appl. Geophys., 139, 338-350.

Portniaguine O. and Zhdanov M.S.; 1999: *Focusing geophysical inversion images*. Geophys., 64, 874-887.

Ray A., Key K., Bodin T., Myer D. and Constable S.; 2014: *Bayesian inversion of marine CSEM data from the Scarborough gas field using a transdimensional 2-D parametrization*. Geophys. J. Int., 199, 1847-1860.

Reid A.B. and Thurston J.B.; 2014: *The structural index in gravity and magnetic interpretation: errors, uses, and abuses*. Geophys., 79, J61-J66.

Reid A.B., Allsop J.M., Granser H., Millett A.T. and Somerton I.W.; 1990: *Magnetic interpretation in three dimensions using Euler deconvolution*. Geophys., 55, 80-91.

Reid A.B., Ebbing J. and Webb S.J.; 2014: *Avoidable Euler errors-the use and abuse of Euler deconvolution applied to potential fields*. Geophys. Prospect., 62, 1162-1168.

Rossi L., Reguzzoni M., Sampietro D. and Sansò F.; 2015: *Integrating geological prior information into the inverse gravimetric problem: the Bayesian approach*. In: Proc. VIII Hotine-Marussi Symposium on Mathematical Geodesy, Roma, Italy, pp. 317-324.

Salem A., Furuya S., Aboud E., Elawadi E., Jotaki H. and Ushijima K.; 2005: *Subsurface structural mapping using gravity data of Hohi geothermal area, central Kyushu, Japan*. In: Proc. World Geothermal Congress, Antalya, Turkey, pp. 24-29.

Savaşcin M.Y. and Oyman T.; 1999: *Tectono-magmatic evolution of alkaline volcanics at the Kırka - Afyon - Isparta structural trend, SW Turkey*. Turk. J. Earth Sci., 7, 201-214.

Seillé H. and Visser G.; 2020: *Bayesian inversion of magnetotelluric data considering dimensionality discrepancies*. Geophys. J. Int., 223, 1565-1583.

Silva J.B. and Barbosa V.C.; 2003: *3D Euler deconvolution: theoretical basis for automatically selecting good solutions*. Geophys., 68, 1962-1968.

Singh K.K. and Singh U.K.; 2017: *Application of particle swarm optimisation for gravity inversion of 2.5-D sedimentary basins using variable density contrast*. Geosci. Instrum., Methods Data Syst., 6, 193-198, doi: 10.5194/gi-6-193-2017.

Smith T., Hoversten M., Gasperikova E. and Morrison F.; 2001: *Sharp boundary inversion of 2D magnetotelluric data*. Geophys. Prospect., 47, 469-486.

Stavrev P.Y.; 1997: *Euler deconvolution using differential similarity transformations of gravity or magnetic anomalies*. Geophys. Prospect., 45, 207-246.

Tedla G.E., Van der Meijde M., Nyblade A.A. and Van der Meer F.D.; 2011: *A crustal thickness map of Africa derived*

*from a global gravity field model using Euler deconvolution*. Geophys. J. Int., 187, 1-9, doi: 10.1111/j.1365-246X.2011.05140.x.

Tiryakioğlu I., Özkaymak Ç., Baybura T., Sözbilir H. and Uysal M.; 2018: *Comparison of palaeostress analysis, geodetic strain rates and seismic data in the western part of the Sultandağı Fault in Turkey*. Ann. Geophys., 61, GD335, 14 pp., doi: 10.4401/ag-7591.

Verduzco B., Fairhead J.D., Green C.M. and MacKenzie C.; 2004: *New insights into magnetic derivatives for structural mapping*. The Leading Edge, 23, 116-119.

Virtanen P., Gommers R., Oliphant T.E., Haberland M., Reddy T., Cournapeau D., Burovski E., Peterson P., Weckesser W., Bright J., van der Walt S.J., Brett M., Wilson J., Jarrod Millman K., Mayorov N., Nelson A.R.J., Jones E., Kern R., Larson E., Carey C., Polat İ., Feng Y., Moore E.W., VanderPlas J., Laxalde D., Perktold J., Cimrman R., Henriksen I., Quintero E.A., Harris C.R., Archibald A.M., Ribeiro A.H., Pedregosa F., van Mulbregt P. and SciPy 1.0 Contributors; 2020: *SciPy 1.0: fundamental algorithms for scientific computing in Python*. Nat. Methods, 17, 261-272, doi: 10.1038/s41592-019-0686-2.

Witter J.B., Siler D.L., Faulds J.E. and Hinz N.H.; 2016: *3D geophysical inversion modeling of gravity data to test the 3D geologic model of the Bradys geothermal area, Nevada, USA*. Geotherm. Energy, 4, 14, 21 pp., doi: 10.1186/s40517-016-0056-6.

Yildiz A., Dumlupinar İ., Bağci M., Ulutürk Y., Başaran C. and Erdoğan E.; 2012: *Afyonkarahisar ve* Çevresinin *Depremselliği*. Afyon Kocatepe Üniversitesi Fen ve Mühendislik Bilimleri Dergisi, 12, 1-7.

Zhao C., Yu P. and Zhang L.; 2016: *A new stabilizing functional to enhance the sharp boundary in potential field regularized inversion*. J. Appl. Geophys., 135, 356-366.

*Corresponding author:*     Gökhan Karcıoğlu
                       Geophysical Engineering Department, Engineering Faculty, İstanbul University - Cerrahpaşa
                       Buyukcekmece, İstanbul, Turkey
                       Phone: +90 212 4040300; e-mail: gkarci@istanbul.edu.tr